Journal of Biomedical Optics

SPIEDigitalLibrary.org/jbo

Detection of breast surgical margins with optical coherence tomography imaging: a concept evaluation study

Dan Savastru
Ernest W. Chang
Sorin Miclos
Martha B. Pitman
Ankit Patel
Nicusor Iftimia

SPIE

Detection of breast surgical margins with optical coherence tomography imaging: a concept evaluation study

Dan Savastru,[a] Ernest W. Chang,[b] Sorin Miclos,[a] Martha B. Pitman,[c] Ankit Patel,[b] and Nicusor Iftimia[b,*]
[a]National Institute of Optoelectronics, 409 Atomistilor Street, Magurele, Ilfov, RO-077125, Romania
[b]Physical Sciences Inc., 20 New England Business Center Drive, Andover, Massachusetts 01810
[c]Massachusetts General Hospital, 55 Fruit Street, Boston, Massachusetts 02114

Abstract. This study aimed to evaluate the concept of using high-resolution optical coherence tomography (OCT) imaging to rapidly assess surgical specimens and determine if cancer positive margins were left behind in the surgical bed. A mouse model of breast cancer was used in this study. Surgical specimens from 30 animals were investigated with OCT and automated interpretation of the OCT images was performed and tested against histopathology findings. Specimens from 10 animals were used to build a training set of OCT images, while the remaining 20 specimens were used for a validation set of images. The validation study showed that automated interpretation of OCT images can differentiate tissue types and detect cancer positive margins with at least 81% sensitivity and 89% specificity. The findings of this pilot study suggest that OCT imaging of surgical specimens and automated interpretation of OCT data may enable in the future real-time feedback to the surgeon about margin status in patients with breast cancer, and potentially with other types of cancers. Currently, such feedback is not provided and if positive margins are left behind, patients have to undergo another surgical procedure. Therefore, this approach can have a potentially high impact on breast surgery outcome. [DOI: 10.1117/1.JBO.19.5.056001]

Keywords: optical coherence tomography imaging; breast cancer; histopathology; positive margins.

Paper 140069RR received Feb. 4, 2014; revised manuscript received Apr. 3, 2014; accepted for publication Apr. 7, 2014; published online May 1, 2014.

1 Introduction

Breast cancer is one of the most common cancers found in women and the second leading cause of cancer deaths after lung cancer.[1] As with all malignancies, early detection of breast cancer is the only way to effectively manage patients who suffer from this disease. According to the American Cancer Society, the five-year survival rates for women with breast cancer who are appropriately treated are as follows: 100% for stage 0, 100% for stage I, 92% for stage IIA, 81% for stage IIB, 67% for stage IIIA, 54% for stage IIIB, and 20% for stage IV.[2] Therefore, improved methods are needed to detect and treat this cancer in its early stage when survival rates are high.

Most patients diagnosed with early-stage breast cancer choose to undergo breast conserving surgery (BCS). This method of treatment is also known as a lumpectomy and involves the local removal of the breast cancer (ideally) with clear tumor-free margins. However, removal of breast cancer with BCS, even when followed by radiation therapy, may not be successful in controlling breast cancer recurrence because microscopic amounts of tumor tissue can be left at the surgical bed, increasing the probability of cancer recurrence.[3–9] One way to avoid this problem is to perform intraoperative evaluation of the surgical margins.

Current techniques for intraoperative pathologic assessment involve touch prep of the lumpectomy perimeter onto glass slides to assess for cancer cells and frozen section analysis of shaved peripheral margins.[10] Touch prep seems to be marginally effective in detecting positive margins, while frozen section assessment is fraught with problems.[11,12] Breast specimens have a high percentage of fat tissue, and thus, they are very difficult to freeze and cut in thin slices for histopathological analysis during the surgery. In addition, freezing artifact hampers optimal evaluation of the tissue for cancer cells following routine processing. Therefore, in most cases, the lumpectomy specimen is sent to the pathology laboratory for routine histology without intraoperative analysis of the surgical margins. A survey of breast surgeons found that no intraoperative assessment is completed in 52% of patients, frozen section is used by 28%, and touch prep by 15%.[11]

Techniques used to make the extent of the tumor more evident to the surgeon during lumpectomy include the hematoma-directed ultrasound-guided technique,[13] intraoperative ultrasound,[14] and dye injection at the tumor site.[15] Each of these techniques has had minimal impact in reducing positive margin rates. In addition, these techniques require the patient to undergo additional procedures that carry further risk and discomfort.

Optical methods have been tested as well for identifying tissue types with the idea of using them for surgical guidance. Among various techniques developed to date, spectroscopic-based methods have shown real promise for tissue-type discrimination.[16–28] However, the resolution of the diffuse reflectance or fluorescence spectroscopy methods is limited, and thus, they can only detect relative large areas of cancer infiltrations on the surgical specimen margins. The use of fiber optic probes helped to identify cancer infiltration at lower scale.

*Address all correspondence to: Nicusor Iftimia, E-mail: iftimia@psicorp.com

0091-3286/2014/$25.00 © 2014 SPIE

Pioneering optical studies were carried out by Bigio et al.[29] However, the drawback of this approach is its very limited field of view, and therefore, it is time consuming when surveying large-size specimens.[30] Raman spectroscopy has also shown promise in detecting tumor sites.[31,32] Unfortunately, Raman imaging is very slow and, thus, not adequate for intraoperative use. More recently, optical coherence tomography (OCT) and its higher-resolution variant, full-field OCT (FFOCT), have been applied to tissue discrimination with the goal of providing an optical biopsy[33] as a means for aiding diagnosis or even guiding biopsies or surgeries in various organs.[34–45] For example, Hsiung et al.[41] has shown that OCT may be used to differentiate between benign and malignant lesions in the human breast. Zhou et al.[42] have evaluated the complementarities of OCT and optical coherence microscopy (OCM) for differentiating between normal and cancer breast specimens. The two imaging modalities have been integrated into one instrument. OCM provided complementary information to OCT images, allowing tracking features from different levels to identify low-contrast structures that were difficult to appreciate from single images alone. More recently, Assayag et al.[43] have investigated the use of large-field, high-resolution FFOCT for evaluating human breast specimens. Although FFOCT provides enhanced resolution compared to OCT, its penetration depth is limited to a few hundred of microns. McLaughlin et al.[44] have shown OCT probe implementation into a hypodermic needle, thus making it possible to differentiate tissue types at the biopsy site. All these studies demonstrate the potential of OCT for differentiating between tissue types and helping clinicians to provide more reliable diagnosis.

Since OCT is capable of imaging tissue structure to a depth of the order of 1.5 to 2 mm at a very high speed (nowadays hundreds of frames per second are possible) and has a decent instantaneous field of view (up to 15×15 mm with large field of view objectives), it might be a more suitable tool than OCM or FFOCT for investigating surgical specimens for cancer presence at the margins. However, one of the important technological aspects toward achieving this goal is to rapidly analyze a large surgical specimen, automatically interpret the OCT data in real time, and provide the results to the surgeon in a very simple and easy to comprehend manner. Trying to reach toward this goal, we present in this paper a preliminary study on the use of an OCT-based approach for rapid collection and nonbiased automated analysis of surgical specimens. Preliminary evaluation of this approach on a mouse model of breast cancer is discussed in detail.

2 Materials and Methods

2.1 *Instrumentation*

A typical OCT instrument based on the Fourier domain spectral approach (see simplified schematic in Fig. 1) was chosen to investigate small animal surgical specimens for presence of cancer positive margins. This instrument uses a 1310 nm superluminescent diode (Exalos, Austria) with a bandwidth of 78 nm as light source. The theoretical axial resolution provided by this source is of the order of 7 μm in tissue ($\Delta z = 0.44\lambda^2/n\Delta\lambda$, where $\Delta\lambda$ is the bandwidth of the light source and n is the refractive index of tissue). Light from this diode is sent to the Michelson interferometer through a fiber optic circulator, which helps to maximize the light collected back from the sample. The retro-reflected light from the sample and reference arm of the interferometer is combined by the 2×2 fiber optic splitter and an interference pattern is obtained when the two arms of the

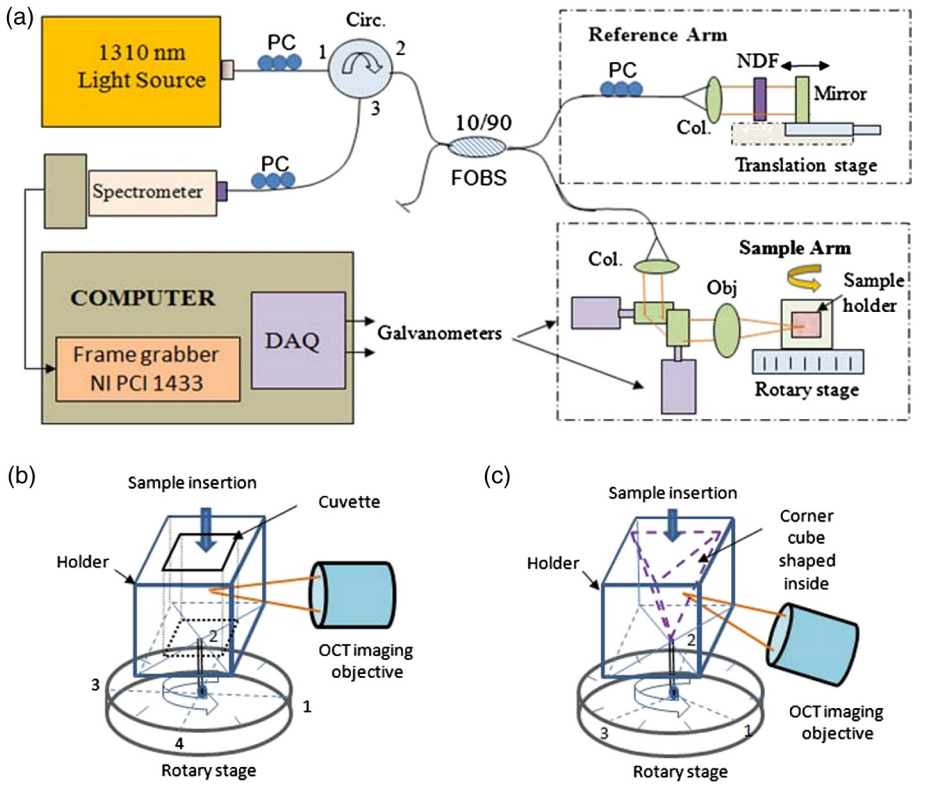

Fig. 1 (a) Simplified schematic of the optical coherence tomography (OCT) instrument. (b) Schematic representation of the tissue holder. (c) Initial design of a holder for larger tissue specimens.

interferometer are matched within the coherence length of the light source. The light collected by the spectrometer is dispersed by a diffraction grating (1200 lines/mm) and projected onto a linear array detector (SUI 1024 LDH2, Sensors Unlimited, New Jersey). In this way, the modulated spectrum carrying the depth information of the investigated sample is obtained. The custom-designed spectrometer (Wasatch Photonics, North Carolina) provides a spectral resolution $\delta\lambda$ of ~0.1 nm, which was used necessarily to allow for a reasonable imaging range $\Delta z \geq 3.0$ mm ($\Delta z_{6\ \mathrm{dB}} = 0.22\lambda^2/\delta\lambda$). The electrical signal from the output of the linear array detector is processed to extract sample depth information (reflectivity profile).

The imaging arm of the instrument was designed to enable rapid investigation of the tissue specimens and provide correlation of the images with the anatomical site. It consists of a scanning engine (6210 galvanometer pair, Cambridge Technologies, Massachusetts) with 6 mm mirror aperture, and a commercially available 5× magnification scan lens (Thorlabs, Newton, New Jersey, Model LSM03) with an effective focal length of 36 mm. This lens allows for tissue imaging with a lateral resolution of the order of 25 μm. A specially designed tissue holder [5 mm cuvette (BrandTech) attached to a rotary mount) was used [see schematic in Fig. 1(b)] to enable rapid imaging of the entire specimen. Normally, on larger specimens, all six facets of the excised lump have to be investigated. However, since the specimens used in our study were rather small (averaging 4 mm), we designed the specimen holder to image four facets only because the imaging depth of OCT (~1.5 mm) is sufficient to resolve the thickness of specimens and, thus, to incorporate the information from the two orthogonal facets.

For larger specimens, a corner cube cup holder can be used [see preliminary design in Fig. 1(c)] and rotated in three sequential positions to enable rapid examination of first three tissue facets, while the remaining three facets can be examined by flipping the tissue specimen inside of the cup. This holder design will be adopted for the OCT instrument planned to be used in subsequent human studies.

2.2 *Animal Model*

A tumor xenograft animal model was used in this study. The xenograft models are widely used to investigate the factors involved in malignant transformation, invasion, and metastasis, as well as to examine response to therapy.[45] In such models, human tumor cells are transplanted into immunocompromised mice that do not reject human cells.

Following the procedures reported by other investigators for developing xenograft models,[45] we developed an animal protocol that was approved by the Institutional Animal Care and Use Committee. The goal of our study was to develop a model that replicates the development of *in situ* ductal breast carcinoma. Therefore, in order to develop a system that models such breast tumors, we injected aggressive basal MDA-MB-231 human ductal breast carcinoma cells (~10^7 in 200 microL) into the mammary fat pads of severely immunocompromised mice females (four to six weeks old). Since the MDA-MB-231 is a metastatic cell line, the animals have to be sacrificed at a relatively short time after the cancer starts developing. In our case, mice started to develop tumors within three to four weeks since cell implantation. Once the tumor masses reached a size of at least 4 mm in diameter, the animals were considered ready for the proposed study and sacrificed with CO_2 inhalation. The tumors were excised with the intent of leaving negative margins (healthy tissue) around each specimen. In addition to the excised tumors, muscle tissue was also excised and used in the animal study for preliminary testing of the tissue differentiation algorithm. The main reason for this was the insufficient fibrous stromal tissue, which is present in the human breast but not in sufficient quantity in the mouse model used in this study. The muscle tissue is structurally different from tumor tissue, but somewhat closer to stromal tissue in terms of scattering properties, and therefore, this tissue class was chosen as a third tissue class in this preliminary study.

Following the approach of the current clinical procedures where each facet of the surgical specimen is marked with dyes of different colors, such that direct correlation with the anatomical site can be rapidly made by the pathologist, we marked with dyes each surface of the excised specimen.

2.3 *Measurement Protocol*

The specimens were then placed in the cuvette holder such that the colors on the specimens matched those painted on the top area of each facet of the cuvette.

Each tissue sample was kept hydrated in saline solution during the measurements. A small amount of saline was placed in the cuvette to keep the sample moist and minimize the backreflection artifacts caused by the interfaces between the sample surface and cuvette wall. Raster scans (4 mm × 2.5 mm) were taken from each facet of the 20 tissue specimens used in our validation set. Each raster contained 250 OCT frames corresponding to a sampling step of 10 microns (250 frames × 10 microns = 2.5 mm, which was our size of the C scan). Each OCT data set was associated to the dye color of the marked surface, such that histology correlation can be performed after completing the OCT measurements. Histologic preparation consisted of specimen fixation, H&E staining, embedding in paraffin, and cutting of 2-mm-thick slices along each surface. Then each subspecimen was cut in slices along the OCT B-scan direction. Finally, histopathology results were compared with OCT findings.

2.4 *Data Processing*

A specially designed signal processing scheme, presented in detail elsewhere,[41] was used to differentiate tissue types by analyzing all the 1024 reflectivity profiles from each image. The processing scheme processes each reflectivity profile (axial-line or A-line) and derives a set of four parameters based on signal intensity and variance directly from the reflectivity profile, as well as a set of two parameters from the Fourier analysis of this signal.

First, the slope of the reflectivity profile is calculated. It provides information related to the depth attenuation of the signal, which is a function of tissue optical properties. Different slopes at different depths might indicate the presence of two or more tissue types within the same depth reflectivity profile. Therefore, linear fitting is performed on several windows, each window corresponding to a portion of the depth reflectivity profile that has the same slope. When different slopes are found within the same A-line, all the subsequent parameters are calculated in each window that was found in this initial step of the signal processing algorithm.

Second, the standard deviation (Std) of the depth profile variations around the linear fit is calculated. These variations may provide information about the scattering characteristics of the

tissue being investigated. Adipose tissue produces strong reflection peaks with low reflectivity zones between them because of the relatively high differences between the refractive indices of the fat cell cytoplasm and membrane, while fibrous and tumor tissues produce lower peaks. Since the mean distance between these peaks is expected to be a characteristic size of the cell size and distance between the cells, the MeanPeakDistance is used as a third parameter. This parameter is expected to be relatively large for adipose tissue, medium for fibrous tissue, and small for tumor, since tumor cells are very densely packaged making the tissue stiffer. The fourth parameter is the standard deviation of the peak spreading over depth (StdPeakDistance). A more homogeneous tumor tissue is expected to have a reduced spread of the peaks than a heterogeneous one. The next two parameters are obtained from the Fourier analysis of the OCT signal. Therefore, power spectrum calculation is the next step in our signal processing algorithm. The power spectrum is normalized to its maximum and a peak detector is used to identify the main frequency components of the spectrum or frequency peaks. The weighted mean frequency (MeanFrequency) and the area of the peaks (PeakArea) are the last two parameters that are evaluated. The power spectrum is expected to have a dominant small frequency for adipose tissue corresponding to large spatial distances between the fat cell walls, while for tumors it is expected to exhibit multiple high frequencies (a broad spectrum with relatively high mean and standard deviation). The peak area is calculated with the purpose of identifying the spread of the dominant frequencies. Sharp peaks (smaller area) or broad peaks (larger area) for the same number of dominant frequencies may indicate the presence of different tissue types within the reflectivity profile. For example, breast cancerous tissue is generally denser and stiffer than the surrounding tissue, and therefore, the OCT signal exhibits an increased number of dominant frequencies resulting in a broad normalized spectrum with large PeakAreas.

The calculated parameters are compared with the mean values of these parameters previously calculated from training sets of adipose, fibrous, and tumor tissues.

The mean value $\bar{x}_i$ of each tissue class from the training set is a column vector with six elements. Covariance matrices are also calculated for each tissue type accounting for all six parameters derived from each A-line.

$$S_i = \frac{1}{n_i}\sum_{j=1}^{n_i}(x_{i,j} - \bar{x}_i)(x_{i,j} - \bar{x}_i)^{\mathrm{T}}, \tag{1}$$

where n_i is the number of elements in each tissue class within the training set and the superscript T indicates matrix-transpose.

For each sample to be diagnosed, the mean values and the covariant matrices are used to calculate a quadratic discrimination score.

$$d_i^Q = -\frac{1}{2}\ln|S_i| - \frac{1}{2}(x - \bar{x}_i)^{\mathrm{T}} S_i^{-1}(x - \bar{x}_i), \tag{2}$$

where $|S_i|$ indicates the matrix determinant, S_i^{-1} is the inverse matrix of S_i, and x is the column vector made of the six calculated parameters for that sample. Three quadratic discrimination scores are obtained for each pixel corresponding to the three tissue classes and the maximum score is selected to assign each pixel of the image to the correct tissue type. The quadratic discrimination score is the logarithm of the probability that the tissue at that pixel belongs to a tissue class and the maximum probability is used for tissue assignment.

This algorithm was applied to every A-line in the OCT image. However, since speckle noise and backreflections from tissue surface can create artifacts, a 25 A-lines neighboring averaging was applied to eliminate such artifacts.

3 Results

The collected OCT data were processed with the goal of identifying the presence of cancer positive margins. Again, a cancer positive margin is an area of the tissue specimen where cancer cells are still present on the surface proximity (within a depth of maximum 2 mm from the surface).

The processing algorithm presented in brief above was used in our analysis. The algorithm was first trained on multiple sets of OCT images. Multiple images for each tissue type (cancer, fat pad, and muscle) were taken from the 10 tissue specimens with known histology (training set). The training set was established with direct feedback from a pathologist, who analyzed the histology of the imaged specimens, so that a direct correspondence between tissue type and OCT data was obtained. Representative cases of OCT images of the three major tissue classes used in our evaluation (adipose, muscle, and cancer) are shown in Fig. 2.

As seen in Fig. 2(a), the adipose tissue consisted of large fat cells, >50 microns in size. The relatively large difference between the refractive indices of the membrane and cytoplasm makes the fat cells easy to be differentiated with OCT. The cell's membrane scatters light intensively, while the cytoplasm does not. Therefore, the cytoplasm shows up dark in the OCT image. The images of the fibrous tissue (muscle in this case) showed the organization of the fiber bundles in those cases where the OCT frame was taken in a plane perpendicular to the muscle fiber bundles [see Fig. 2(b)]. However, when the OCT imaging frame was taken along the muscle fiber bundles, the striations were no longer visible [see Fig. 2(c)]. This is the case when even a highly trained OCT reader may not be able to recognize the nature of the investigated tissue specimen. The OCT images of the cancer infiltrated tissue [see Fig. 2(d)] showed relatively uniform scattering, which decreases with depth. This seems to be caused by the enlarged nuclei, which make the tissue both optically and mechanically denser. The enhanced scattering and the absorption of the dense microvasculature feeding the tumor cells contribute to smaller penetration depth than in the case of muscle or fibroadipose tissue.

The differentiation of tissue type becomes more difficult when more than one tissue type is present within the same OCT frame. It is already known that breast tumor tissue is usually very heterogeneous (cancer cells are admixed with adipose or fibroadipose cells). Therefore, even a highly trained OCT reader may have a hard time to reliably detect the presence of infiltrated cancer in fibroadipose tissue.

To eliminate OCT reader subjectivity, our approach was to analyze each tissue reflectivity profile (A-line) within the OCT image instead of defining criteria for tissue differentiation based on specific texture features. In our earlier research,[36,37] we found that breast tissue types can be reliably differentiated by analyzing various metrics of the reflectivity profiles of the tissue. A typical example is shown in Fig. 2. By examining the reflectivity profiles of each tissue type [see Figs. 2(a') to 2(d')], one can observe clear differences between the slopes of the profiles, as well as between signal variances. Therefore, as discussed above, our approach was to analyze these reflectivity

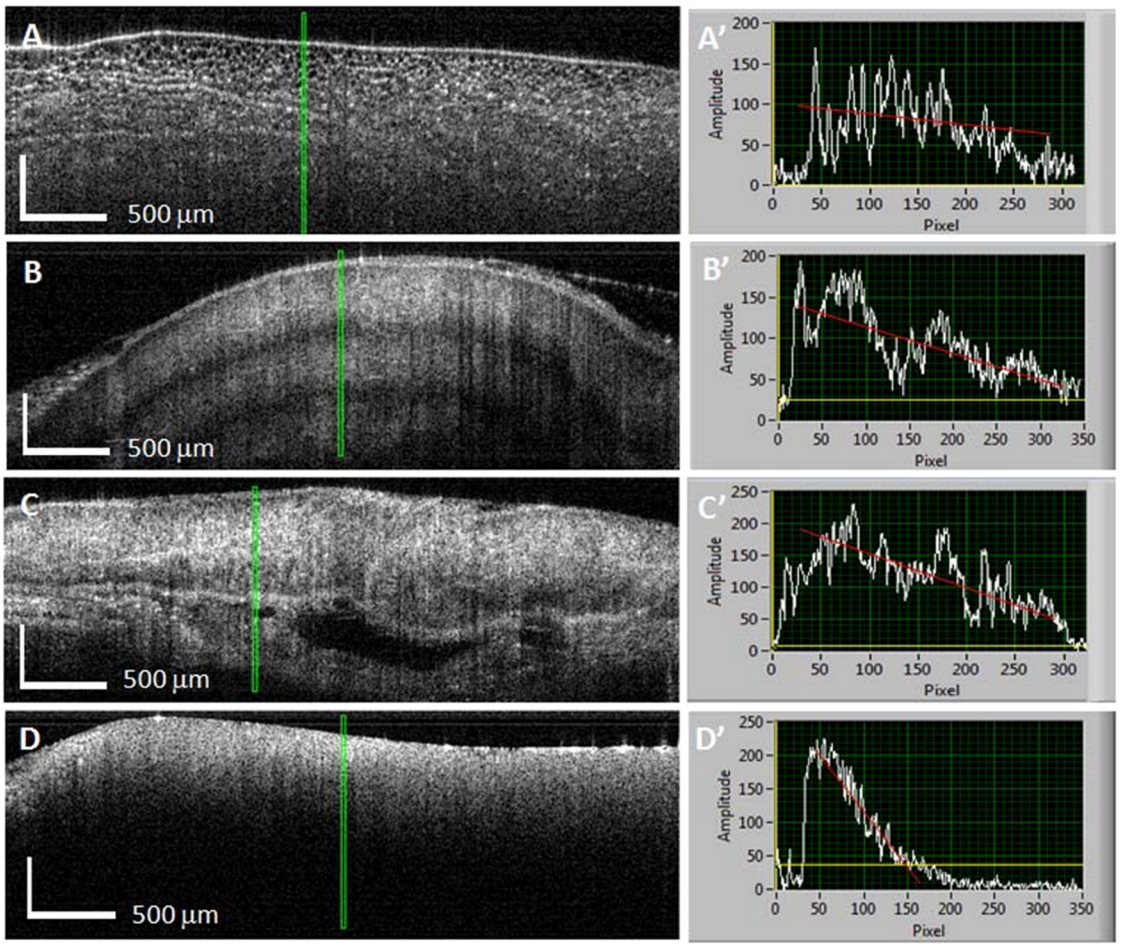

Fig. 2 Representative cases of tissue reflectivity profiles: (a) adipose tissue, (b) and (c) muscle tissue with muscle bundle orientations on perpendicular and parallel planes to the imaging plane, (d) tumor tissue.

profiles and derive several parameters that could be used to substantiate the differences among various tissue types present within the same OCT frame. Specific metrics within each reflectivity profile were derived and compared with those from the training set of tissue types. Our previous studies[40,41] have shown that this approach can provide reliable tissue differentiation and, thus, can be used to eliminate the potential subjectivity of the OCT reader.

Each OCT frame was automatically analyzed with our software algorithm and the findings were correlated with histology results. If at least one single frame was showing cancer infiltrations within the 1-mm margins, the specimen was labeled as having positive cancer margins. Although apparently, after visual examination of each surface, the specimens did not show clear areas of high vascularization or increased mechanical stiffness, which are some of the characteristics of cancer infiltrations within the margins, the processed OCT data have indicated the presence of positive margins (infiltrated cancer cells) on multiple specimens examined in our pilot validation study, as summarized in Table 1.

The analysis was performed accounting for multiple images acquired from each facet of the tissue specimen. The specimens were placed in the cancer negative class or true negative (TN) class when all the processed OCT frames from the four facets of the tissue specimen showed normal healthy tissue (adipose, fibrous, or fibroadipose), and in the true positive (TP) class when at least one frame showed cancer infiltrations within the 1-mm margins. These results of the OCT findings were compared with histopathology results. The miscorrelations were placed in the false negative (FN) class when specimens with tumor infiltrations were attributed by the algorithm to the TN class, and in the false positive (FP) class when specimens with no cancer infiltrations were attributed to the TP class. The overall sensitivity was 81%, while the specificity was 89%. These results suggest that further improvements are still needed in our processing algorithm and possibly in imaging resolution to improve OCT-histology correlation.

Representative cases of our findings are sown in Figs. 3 and 4. Figure 3 summarizes the case of a surgical specimen with adipose appearance of the surgical margins. The CCD images of the surgical specimen did not show any sign of high vascularization or superficial changes in morphology, suggesting that this specimen may have negative (safe) surgical margins. However, the cross-sectional OCT images [see Figs. 3(c) and 3(d)] showed an adipose rim followed by an optically denser tissue, which scatters light intensively, similar to the behavior of cancer tissue analyzed in the training set. The enface OCT image from Fig. 3(b), representing a slice through the specimen at a depth of ~150 μm relative to its surface, also revealed an adipose rim followed by denser tissue. The tissue differentiation

Table 1 Summary of optical coherence tomography (OCT) histology correlation.

		OCT automated analysis findings				
Histology-based diagnosis		Normal adipose	Normal fibroadipose	Adipose with cancer infiltrations	Fibroadipose with cancer infiltrations	Misclassifications
Normal adipose	3	3 TN				100% correlation
Normal fibroadipose	6		5 TN		1 FP	1FP: cancer infiltrations falsely predicted
Adipose with cancer infiltrations	3	1 FN		2 TP		1 FN: cancer infiltrations not detected
Fibroadipose with cancer infiltrations	8		1 FN		7 TP	1 FN: cancer infiltrations not detected
Total specimens	**20**	**Results: 8 TN; 9 TP; 1 FP; 2 FN** **Sensitivity** $= \mathbf{TP}/(\mathbf{TP}+\mathbf{FN}) = 0.81$; **Specificity** $= \mathbf{TN}/(\mathbf{TN}+\mathbf{FP}) = 0.89$				

Note: TN, true negative; FP, false positive; FN, false negative; TP, true positive.

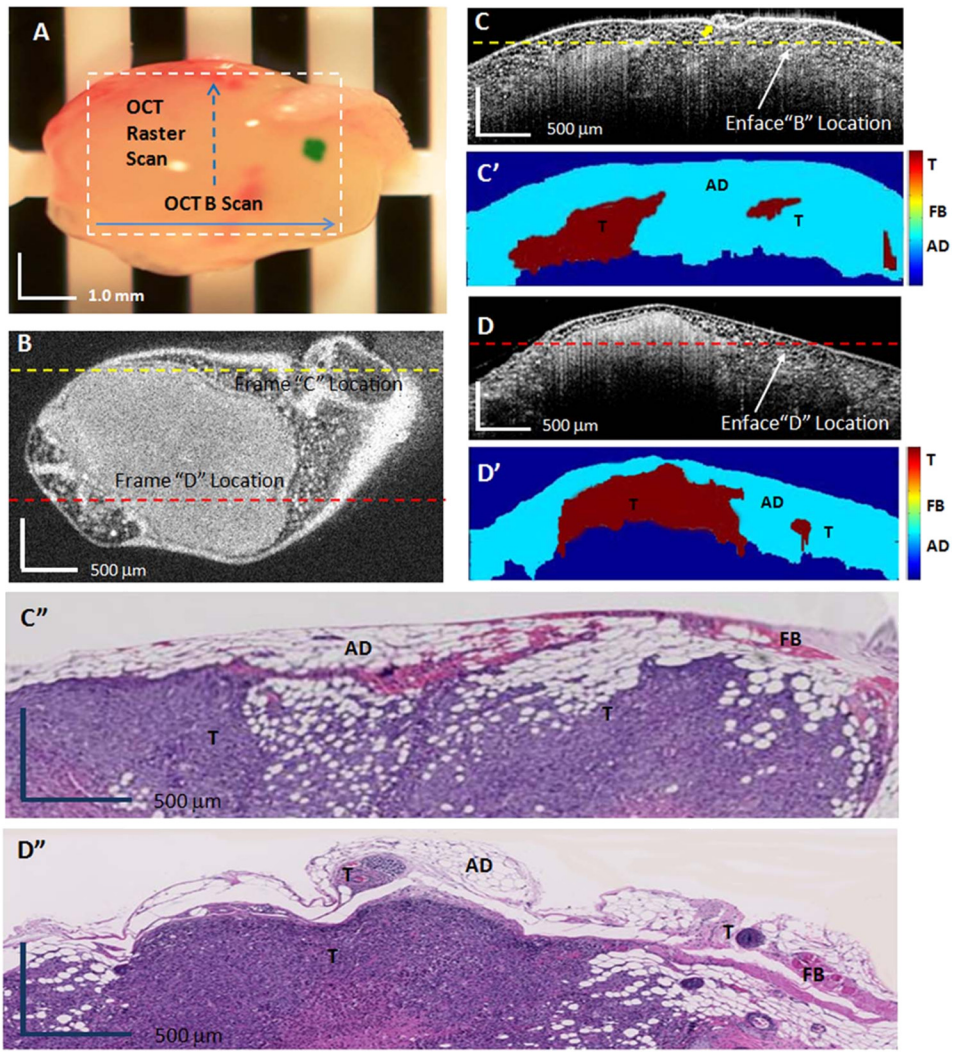

Fig. 3 Representative case of OCT findings on a surgical specimen with adipose appearance of the margins. (a) CCD image of the surgical specimen. (b) Enface OCT image at depth of ~150 μm from its surface. (c) and (d) Cross-sectional OCT images corresponding to the yellow/red-dotted lines from (b). (c') and (d') Tissue type classification maps. (c") and (d") Histological appearance of the specimen on the areas marked with red/yellow-dotted lines in (b).

algorithm indicated cancer presence within the 1-mm margins, as it can be observed from Figs. 3(c') and 3(d'). The tumor, which occupies a large area within the specimen, almost reaches its surface. In addition, some focal infiltrations are present in peripheral or slightly deeper central areas. Similar findings were found on several more frames taken from the other two surfaces of the specimen. These findings were confirmed by the histological analysis, as shown in Figs. 3(c'') and 3(d''). These histological sections show a mass of cancer cells infiltrating the specimen ~0.1 mm beneath the rim of adipose tissue. In a real clinical case, a specimen like this would be categorized as having nonsafe surgical margins. The presence of the cancer cells very close to the specimen surface indicates that some clusters of cancer cells could also have been left in the surgical bed.

Another representative case is shown in Fig. 4 where the gross appearance of the surgical specimen, again, did not show signs of high vascularization or superficial changes in morphology, suggesting that this specimen might have safe surgical margins. The cross-sectional OCT images [see Figs. 4(c) and 4(d)], however, show a very thin adipose layer followed by a thick layer of optically denser fibrotic-like tissue. A rim of adipose cells followed by a bundled muscle-like appearance in Fig. 4(c) suggests that this specimen has a muscular surgical layer underneath the adipose rim. However, the OCT image from Fig. 4(d) shows additional changes in the morphology, especially on the left side of the specimen. The enface image taken at a depth of ~750 μm relative to its surface also indicates the presence of an adipose rim on the top of the image followed by a fibromuscular appearance with some denser infiltrations. Algorithm findings suggest that while the tissue mainly appears noncancerous, small foci of infiltrating tumor (T) are still present within the 1-mm margins, especially on the left sides of the specimen, as indicated in Fig. 4(d'). Histological analysis confirms cancer presence on the second slice [see darker staining at the interface fibrous-adipose, as well as within the adipose layer on Fig. 4(d'')]. Similar features were found on

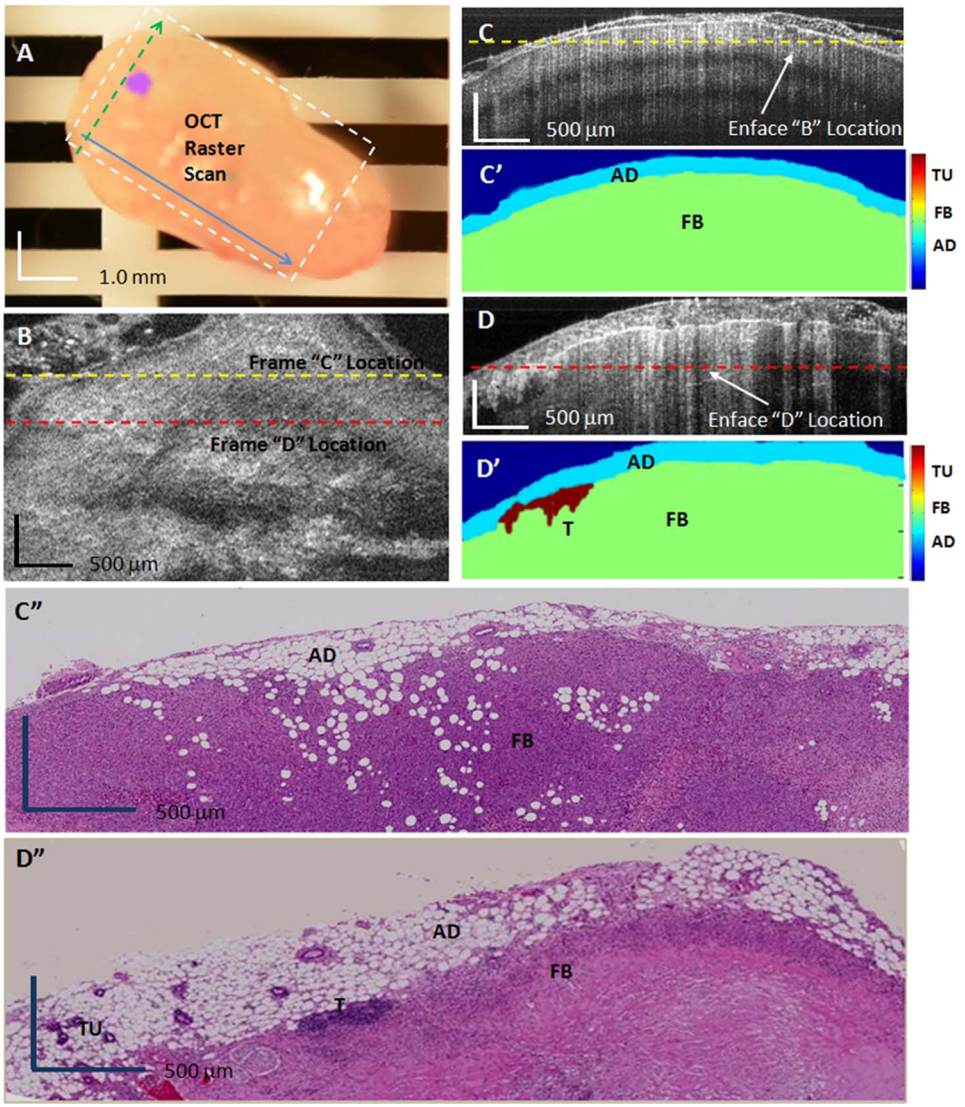

Fig. 4 Representative case of OCT findings on a surgical specimen with fibroadipose-like margins. (a) CCD image of the surgical specimen. (b) Enface OCT image at a depth of ~750 μm from specimen surface. (c) and (d) Cross-sectional OCT images corresponding to the red/yellow-dotted lines from (b). (c') and (d') Tissue type classification maps. (c") and (d") Histological appearance of the specimen (histology slides were cut from the red/yellow-dotted marks in (b).

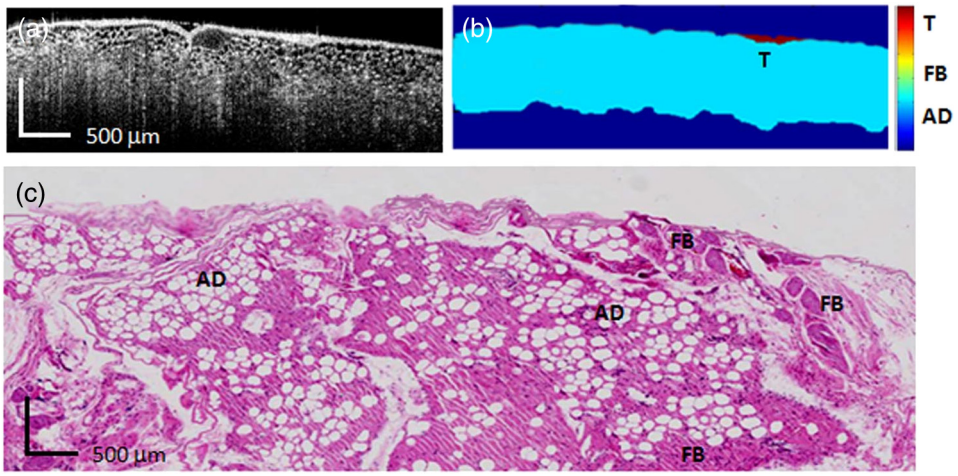

Fig. 5 Representative case of a false positive diagnosis. (a) Cross-sectional OCT frame of a mainly adipose specimen. (b) Tissue classification map. (c) Histology showing the normal adipose appearance with some fibrotic infiltrations.

a few more OCT frames taken from this surface of the specimen. No infiltrations within the 1-mm margins were found on the other three surfaces. Again, the presence of the cancer cells very close to the specimen surface indicates that some clusters of cancer cells could also have been left in the surgical bed.

Although in most of the analyzed cases a good match between the OCT and histology findings was found, in a few cases OCT findings did not match histology, as indicated in Table 1. One of the cases was that of an FP finding, where the algorithm has wrongly estimated cancer presence on a fibroadipose specimen with safe surgical margins (see Fig. 5). The top surface of the specimen had a small fibrotic area. The denser optical appearance of this area was inflated by the specular reflectance, resulting in a magnification of its optical density, which was wrongly interpreted by the algorithm as being cancer. The two FN cases correspond to very small cancer infiltrations in adipose or fibroadipose specimens (see an example in Fig. 6). The FN cases may be attributed to OCT incapability of resolving small infiltration of the cancer cells within the 1-mm margins due to OCT limited axial and lateral resolution. The FP finding may also be attributed to insufficient training of the OCT algorithm. A larger training set might help to better train the algorithm and further minimize the number of FN and FP.

4 Discussion and Conclusions

A novel approach for rapid analysis of the surgical margins is presented. It is based on the OCT scanning of the surgical specimen facets and real-time analysis of the acquired images to determine cancer presence within the margins. A cancer positive margin is an area of the tissue specimen where cancer cells are still present within several millimeters to the surface proximity. Currently, there is no general consensus among surgeons of what the depth of safe surgical margins should be. Some studies suggest that a surgical specimen has to be free of cancer cells on at least 1 mm in depth from its surface,[46] while other studies consider surgical margins >3 mm.[47] However, it is clear that if cancer cells are found within several millimeters from the lumpectomy specimen surface, additional tissue has to be removed to make sure that cancer cells were not left within the surgical bed.

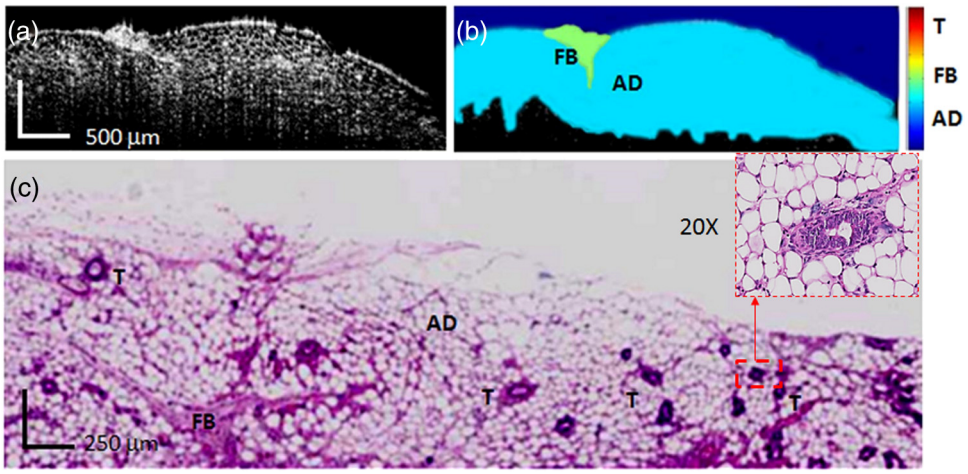

Fig. 6 Representative case of a false negative diagnosis. (a) Cross-sectional OCT frame of a mainly adipose specimen. (b) Tissue classification map. (c) Histology showing the infiltration of the cancer clusters within the 1-mm margin.

A feasibility testing of this approach on mouse animal model of breast cancer was performed. Distinction between normal and cancer tissue was demonstrated with >80% sensitivity and specificity. The automated analysis of the OCT images has proven to quite reliably differentiate between three tissue types: adipose, fibrous, and tumor. The algorithm failed to highlight the presence of cancers within the safe margins (FN) in cases when only a few cells were present within the investigated area. The FN may be reduced if higher axial/later resolution OCT imaging and noise reduction/speckle averaging approaches are used to more reliably pick up cellular-scale tissue features. These improvements on imaging performance might eliminate the need for postprocessing averaging of the algorithm findings on adjacent A-lines. The algorithm has also provided an FP result in the case of a fibroadipose specimen, where a small fibrotic area was labeled as being cancer. The FP/FN findings may be further diminished if a larger training set is used to increase the statistics on the training set parameters.

The tissue differentiation algorithm may be further refined to improve its accuracy by considering the addition of new metrics provided by a complementary optical modality to OCT, such as absorption spectroscopy, fluorescence imaging, Raman spectroscopy, etc., which can be implemented with the same optical instrument to provide coregistered data. It is also to be noted that this algorithm cannot be applied from one organ to another or from animals to humans without establishing a proper training set of tissue types.

Although this approach is offering a notable step forward toward intrasurgical analysis, it is still not suitable for real-time feedback during surgery due to relatively long processing time. The CPU processing time for an individual OCT frame currently takes ~10 s. This processing speed is not adequate when relatively large lumpectomy specimens (>3 cm in size) have to be investigated. The speed of the algorithm could be improved by performing all the calculations in the graphical processing unit. Our preliminary estimate is that a 10-fold increase in the processing speed will be possible.

In summary, we have shown that high-resolution OCT imaging and automated processing of the OCT data can be used to nonsubjectively detect cancer foci on surgical margins that appear grossly normal. Refinement of algorithm to more reliably detect cancer presence, as well as substantial decrease in the processing time may enable the use of this technology to intraoperatively provide real-time feedback to surgeon about margin status in patients with breast cancer, and perhaps in patients with other types of cancer.

Acknowledgments

This research program was funded in part by the Romanian government, Grant No. 184 PCCA/2012 – MOIST, and by U.S. National Cancer Institute, Grant No. 5R42CA114896-04.

References

1. "What are the key statistics about breast cancer?," http://www.cancer.gov/cancertopics/types/breast.
2. "Breast cancer- what are the survival rates?," http://www.nlm.nih.gov/MEDLINEPLUS/ency/article/000913.htm.
3. G. P. Swanson, K. Rynearson, and R. Symmonds, "Significance of margins excision on breast cancer recurrence," *Am. J. Clin. Oncol.* **25**(5), 438–441 (2002).
4. M. Morrow, "Breast conservation and negative margins: how much is enough?," *Breast* **18**(Suppl. 3), S84–S86 (2009).
5. M. Azu et al., "What is an adequate margin for breast-conserving surgery? Surgeon attitudes and correlates," *Ann. Surg. Oncol.* **17**(2), 558–563 (2010).
6. L. Jacobs, "Positive margins: the challenge continues for breast surgeons," *Ann. Surg. Oncol.* **15**(5), 1271–1272 (2008).
7. F. Meric et al., "Positive surgical margins and ipsilateral breast tumor recurrence predict disease-specific survival after breast-conserving therapy," *Cancer* **97**(4), 926–933 (2003).
8. S. L. Blair et al., "Attaining negative margins in breast-conservation operations: is there a consensus among breast surgeons?," *J. Am. Coll. Surg.* **209**(5), 608–613 (2009).
9. L. L. Kestin et al., "Mammographically detected ductal carcinoma in situ treated with conservative surgery with or without radiation therapy: patterns of failure and 10-year results," *Ann. Surg.* **231**(2), 235–245 (2000).
10. F. D'Halluin et al., "Intra-operative touch preparation cytology following lumpectomy for breast cancer: a series of 400 procedures," *Breast* **18**(4), 248–253 (2009).
11. E. K. Valdes et al., "Intra-operative touch preparation cytology; does it have a role in re-excision lumpectomy?," *Ann. Surg. Oncol.* **14**(3), 1045–1050 (2007).
12. J. C. Cendan, D. Coco, and E. M. Copeland III, "Accuracy of intra-operative touch prep frozen-section analysis of breast cancer lumpectomy bed margins," *J. Am. Coll. Surg.* **201**(2), 194–198 (2005).
13. M. Thompson et al., "Hematoma-directed ultrasound-guided (HUG) breast lumpectomy," *Ann. Surg. Oncol.* **14**(1), 148–156 (2007).
14. C. Eichler et al., "Intraoperative ultrasound: improved resection rates in breast-conserving surgery," *Anticancer Res.* **32**(3), 1051–1056 (2012).
15. P. Ananthakrishnan, F. L. Balci, and J. P. Crowe, "Optimizing surgical margins in breast conservation," *Int. J. Surg. Oncol.* **2012**, 585670 (2012).
16. O. Falou et al., "Diffuse optical spectroscopy evaluation of treatment response in women with locally advanced breast cancer receiving neoadjuvant chemotherapy," *Transl. Oncol.* **5**(4), 238–246 (2012).
17. R. R. Alfano et al., "Optical spectroscopic diagnosis of cancer and normal breast tissues," *J. Opt. Soc. Am. B Opt. Phys.* **6**(5), 1015–1023 (1989).
18. R. R. Alfano et al., "Fluorescence-spectra from cancerous and normal human-breast and lung tissues," *IEEE J. Quantum Electron.* **23**(10), 1806–1811 (1987).
19. Y. L. Yang et al., "UV reflectance spectroscopy probes DNA and protein changes in human breast tissues," *J. Clin. Laser Med. Surg.* **19**(1), 35–39 (2001).
20. P. K. Gupta, S. K. Majumder, and A. Uppal, "Breast cancer diagnosis using N-2 laser excited autofluorescence spectroscopy," *Lasers Surg. Med.* **21**(5), 417–422 (1997).
21. N. Ghosh et al., "Measurement of optical transport properties of normal and malignant human breast tissue," *Appl. Opt.* **40**(1), 176–184 (2001).
22. G. M. Palmer et al., "Comparison of multiexcitation fluorescence and diffuse reflectance spectroscopy for the diagnosis of breast cancer," *IEEE Trans. Biomed. Eng.* **50**(11), 1233–1242 (2003).
23. N. Ramanujam, "Fluorescence spectroscopy of neoplastic and non-neoplastic tissues," *Neoplasia* **2**(1–2), 89–117 (2000).
24. N. Shah et al., "Noninvasive functional optical spectroscopy of human breast tissue," *PNAS* **98**(8), 4420–4425 (2001).
25. B. W. Pogue et al., "Quantitative hemoglobin tomography with diffuse near-infrared spectroscopy: pilot results in the breast," *Radiology* **218**(1), 261–266 (2001).
26. B. Pogue et al., "Characterization of hemoglobin, water, and NIR scattering in breast tissue: analysis of intersubject variability and menstrual cycle changes," *J. Biomed. Opt.* **9**(3), 541–552 (2004).
27. G. M. Palmer et al., "Comparison of multiexcitation fluorescence and diffuse reflectance spectroscopy for the diagnosis of breast cancer," *IEEE Trans. Biomed. Eng.* **50**(11), 1233–1242 (2003).
28. S. G. Demos, A. J. Vogel, and A. H. Gandjbakhche, "Advances in optical spectroscopy and imaging of breast lesions," *J. Mammary Gland Biol. Neoplasia* **11**(2), 165–181 (2006).
29. I. J. Bigio et al., "Diagnosis of breast cancer using elastic-scattering spectroscopy: preliminary clinical results," *J. Biomed. Opt.* **5**(2), 221–228 (2000).
30. C. F. Zhu et al., "Use of a multiseparation fiber optic probe for the optical diagnosis of breast cancer," *J. Biomed. Opt.* **10**(2), 024032 (2005).

31. A. S. Haka et al., "In vivo margin assessment during partial mastectomy breast surgery using Raman spectroscopy," *Cancer Res.* **66**(6), 3317–3322 (2006).
32. A. S. Haka et al., "Diagnosing breast cancer by using Raman spectroscopy," *Proc. Natl. Acad. Sci. U.S.A* **102**(35), 12371–12376 (2005).
33. M. Zysk and S. A. Boppart, "Computational methods for analysis of human breast tumor tissue in optical coherence tomography images," *J. Biomed. Opt.* **11**(5), 054015 (2006).
34. F. T. Nguyen et al., "Intraoperative evaluation of breast tumor margins with optical coherence tomography," *Cancer Res.* **69**(22), 8790–8796 (2009).
35. B. D. Goldberg et al., "Automated algorithm for differentiation of human breast tissue using low coherence interferometry for fine needle aspiration biopsy guidance," *J. Biomed. Opt.* **13**(1), 014014 (2008).
36. N. V. Iftimia et al., "A portable, low coherence interferometry based instrument for fine needle aspiration biopsy guidance," *Rev. Sci. Instrum.* **76**(6), 064301 (2005).
37. J. M. Schmitt, A. Knuttel, and R. F. Bonner, "Measurement of optical-properties of biological tissues by low-coherence reflectometry," *Appl. Opt.* **32**(30), 6032–6042 (1993).
38. S. A. Boppart et al., "Optical coherence tomography: feasibility for basic research and image-guided surgery of breast cancer," *Breast Cancer Res. Treat.* **84**(2), 85–97 (2004).
39. N. Iftimia et al., "Spectral-domain low coherence interferometry/optical coherence tomography system for fine needle breast biopsy guidance," *Rev. Sci. Instrum.* **80**(2), 024302 (2009).
40. M. Mujat et al., "Automated algorithm for breast tissue differentiation in optical coherence tomography," *J. Biomed. Opt.* **14**(3), 034040 (2009).
41. P. L. Hsiung et al., "Benign and malignant lesions in the human breast depicted with ultrahigh resolution and three-dimensional optical coherence tomography," *Radiology* **244**(3), 865–874 (2007).
42. C. Zhou et al., "Integrated optical coherence tomography and microscopy for ex vivo multiscale evaluation of human breast tissues," *Cancer Res.* **70**(24), 10071–10079 (2010).
43. O. Assayag et al., "Large field, high resolution full-field optical coherence tomography: a pre-clinical study of human breast tissue and cancer assessment," *Technol. Cancer Res. Treat. Express* **1**(1), 21–34 (2013).
44. R. A. McLaughlin et al., "Imaging of breast cancer with optical coherence tomography needle probes: feasibility and initial results," *IEEE J. Sel. Topics Quantum Electron.* **18**(3), 1184–1191 (2012).
45. E. Iorns et al., "A new mouse model for the study of human breast cancer metastasis," *PLoS One* **7**(10), e47995 (2012).
46. T. A. Stamey et al., "Positive surgical margins at radical prostatectomy: importance of the apical dissection," *J. Urol.* **143**(6), 1166–1172 (1990).
47. "Controversial study suggests large margins reduce recurrence risk," http://www.breastcancer.org/research-news/20120322.

Biographies of the authors are not available.